Spring 4-13-2023

Evaluation of the Dynamic Vision Sensor's Photoreceptor Circuit for Infrared Event-Based Sensing

Zinah M. Alsaad

"Evaluation of the Dynamic Vision Sensor's Photoreceptor Circuit for Infrared Event-Based Sensing" a thesis prepared by Zinah M. Alsaad in partial fulfillment of the requirements for the degree, Masters of Science, has been approved and accepted by the following:

Dr. Payman Zarkesh-Ha
Director, Center for High Technology Materials
Professor, Department of Electrical and Computer Engineering

Date

Committee in charge:

Dr. Payman Zarkesh-Ha

Dr. Francesca Cavallo

Dr. Preston T. Webster

EVALUATION OF THE DYNAMIC VISION SENSOR'S PHOTORECEPTOR CIRCUIT FOR INFRARED EVENT-BASED SENSING

BY

Zinah M. Alsaad, B.S. University of New Mexico

Submitted in partial fulfillment of the requirements

for the degree

Masters of Science

Electrical Engineering

University of New Mexico

Albuquerque, New Mexico

May 2023

ACKNOWLEDGMENTS

I would like to thank my advisor, Dr. Payman Zarkesh-Ha, for his encouragement and constant technical and academic support. I would also like to thank Dr. Preston T. Webster from Air Force Research Laboratory/Space Vehicles Directorate for his constant guidance and advisement throughout this thesis, Dr. Francesca Cavallo for her support and recommendations for the various issues that arose, Dr. Julie V. Logan, Dr. Chritian P. Morath, and the AFRL/RVSU Advanced Electro-Optical Space Sensors (AEOSS) group. I would like to acknowledge and thank the professors of the electrical and computer engineering department who provided me a strong foundation in my engineering career thus far. Last but not least, I would like to thank my number one support team who were there since day one; Mom, Dad, my sisters Basma and Tiba.

This work has benefited from the financial support of the US Department of Defense SMART Fellowship, as well as financial support from the Air Force Research Laboratory Space Vehicles Directorate.

Zinah M. Alsaad

EVALUATION OF THE DYNAMIC VISION SENSOR'S PHOTORECEPTOR CIRCUIT FOR INFRARED EVENT-BASED SENSING

by

Zinah M. Alsaad

B.S. Electrical Engineering, University of New Mexico, 2022

M.S. Electrical Engineering, University of New Mexico

ABSTRACT

For space surveillance applications, neuromorphic imaging is being studied as it may perform sensing and tracking tasks with less power and downstream datalink demand. The read-out of the event-based camera is made to only be sensitive to changes in the signals it receives from the photodetector, which results in a datastream of events indicating where and when changes in illumination occur. This is in contrast to the conventional framing camera, which produces images by essentially counting the electrons produced by light incident on each pixel's photodetector. These cameras are commercially available with silicon-based detectors for applications involving visible wavelengths. However, much more research is needed before the event-based read-out can be effectively used with smaller bandgap photodetectors to increase the utility of event-based sensing into the mid- and long-wavelength infrared.

The photoreceptor stage is the main part of the event-based read-out circuitry that interacts with the photodetector. To evaluate the performance and limitations of using pixel circuitry for longer wavelength infrared detection, DC and AC characterizations of the event-based sensor photoreceptor circuit are conducted as a function of mid-wave infrared detector parameters. Detailed analysis of the circuit provides insight into the sensitivity of the photodetector bias stability, the temperature-dependence of the dynamic range, practical constraints to the dynamic range that emerge with the use of longer-wavelength photodetectors, and bandwidth dependence on the input photodetector current. The purpose of this study is to develop a fundamental event-based sensing circuit that is tailored for mid-wave infrared photodetection. This will allow for the characterization of prototype mid-wave event-based sensors and enable the evaluation of which mid-wave infrared detector properties significantly impact the event-based sensor's performance characteristics.

CONTENTS

1 Introduction

Conventional frame-based sensor technologies have dominated the space-based sensing industry for decades. While traditional CCD/CMOS sensing technologies are highly effective at extracting information from data composed of sequential image frames, this methodology presents issues and constraints. For example, the resolution of higher-speed temporal information in the scene necessitates higher frame rates. This results in correspondingly higher data communication capacity requirements which already exceed 1 GB/s for an 8k $\times$ 8k focal plane array with a 16-bit message size operating at even a modest frame rate of 10 Hz [1]. To use a frame-based camera for target tracking applications, all of the frame data must be processed to maintain continuous scene monitoring, taxing satellite communication bandwidth, and on-board power resources processing what is often highly redundant information (that is, information that is not changing with time). The negative impacts of tracking operations within the frame-based imaging paradigm will only continue to rise with increasing spatial and temporal resolution requirements [2]. However, in mission areas where only the dynamic scene information is of interest, the inherently compressed data and high dynamic range of an event-based sensor (EBS) may better serve this role in an ever-growing and interconnected sensing network.

The fundamental EBS pixel design consists of three main stages: photo-

receptor, differentiating circuit, and two comparators. Similar to the human eye, the photo-receptor stage is the first stage of the circuitry that logarithmically compresses the input current by introducing a load resistance through a MOSFET (Metal Oxide Semiconductor Field Effect Transistor) [3], in each pixel to then be differentiated with respect to the last value that triggered an event. This change of illumination enters the final stage to be compared to positive and negative contrast threshold values and turned into true or false events, should one of the thresholds be met [4].

While interest in using event-based sensors in the space domain is growing, a key technological obstacle to their adoption for many applications is the spectral response of their pixel's photodetector, which is silicon-based in all commercially-available EBS cameras to date and thus limited to detecting in the visible and near-infrared. This study extends the utility of EBS to longer wavelength applications; the functionality of the standard 3-stage EBS pixel unit cell must be analyzed, starting with the stage that directly interacts with the photodetector element; the photoreceptor is analyzed for mid-wave infrared (MWIR) event-based sensing by simulating the photoreceptor stage output for III-V MWIR detector parameters, and examining the limitations of the circuitry. For example, unlike diffusion-limited silicon photodiodes where increasing the reverse biasing voltage has near-zero effect on the dark current [12], longer wavelength IR detectors can be much more sensitive to bias voltage variations [13], introducing a potential source

of feedback in the circuit. Instability in detector bias could produce a variation in voltage at the output of the photoreceptor stage and potential false-events if the circuit is not designed with the characteristics of the photodetector in mind. Additionally, the magnitude of dark current in a mid-wave infrared (MWIR) detector is substantially larger than that of a Si detector, necessitating operation at lower temperatures. Lower temperature operation increases the maximum potential dynamic range of the EBS; however, the detector's dark current would ultimately set a practical limit to the dynamic range. Understanding the limitations of the EBS pixel design will provide insight into the relevant figures of merit of the circuitry for infrared applications, how the design can be modified to accommodate requirements best, and the fundamental performance limitations in this implementation of the unit cell.

2 Background

2.1 Event-Based Sensors

Event-based sensors (EBS) provide a low pixel rate mismatch, wide communication bandwidth, and low latency [3] by having each pixel asynchronously respond to the change of illumination levels with respect to background illumination, essentially imitating biological vision. While sensing technologies have become highly effective at extracting information from sequential scene frames, the nature of this methodology presents many issues and constraints. The limitations, such as communication bandwidth and power consumption, are all due to the continuous computation and processing of incoming data even for a static scene. Efforts to reduce these limitations by minimizing incoming data are pushing us towards low power and wide dynamic range event-based imaging.

Figure 1 plots the incoming data-stream from an EBS camera (solid line) sending an approximate 10 Mb/s of data for a 720 x 600 video, in comparison to a frame based camera (dashed line) which produces 1187 Mb/s for the same video. The difference of the amount of data produced in this example demonstrates the impact of using EBS over other conventional imaging forms. This difference drastically reduces computational requirements, bandwidth, and power consumption.

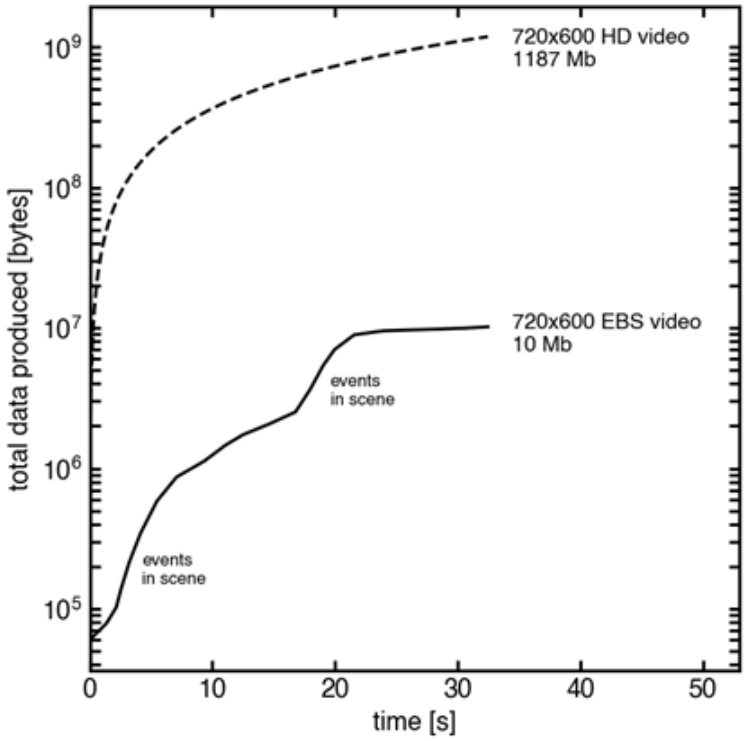

Figure 1: Conventional vs Event-Based Datastream, showing the data produced by each imager as a function of time for the same 720 x 600 video. The figure is used with permission of Julie V. Logan

2.2 Infrared Detectors

Infrared detectors used in space must meet a unique set of performance standards than those used elsewhere.This stems from their low photon irradiance environment, requiring low dark current and noise equivalent irradiance, both of lower temperature operation. Due to the depletion dark currents coming from the absorbing material, barrier infrared detectors perform better for mid- to long-wavelength infrared sensing [15]. In this study, an nBn mid-wavelength infrared detector response is used as an input for the EBS circuitry.

Figure 2 plots the dark current density of a 5.5 μm cutoff nBn infrared detector at temperatures ranging from 80K to 100K to illustrate the importance of tuning the photoreceptor circuit for the characteristics of the MWIR photodetector. The 0.2 V reverse bias operating point indicated on the black curve is selected to yield the lowest shot noise equivalent irradiance at 130 K [10], and the magnitude of dark current density at this voltage 2.1 $\mu A/cm^2$, which is near the median value for these detectors based on measured data on nBns and within a factor of 3$\times$ of the Rule 07 [9] expectation indicated by the horizontal black solid line.

Capacitance vs voltage measurement is considered to be a reliable method in extracting the doping profiles in devices [16]. Additionally, the values make a significant impact on EBS performance metrics such as bandwidth which will be discussed in section 5.2. Fig. 3 plots the capacitance density of a 5.5 μm cutoff

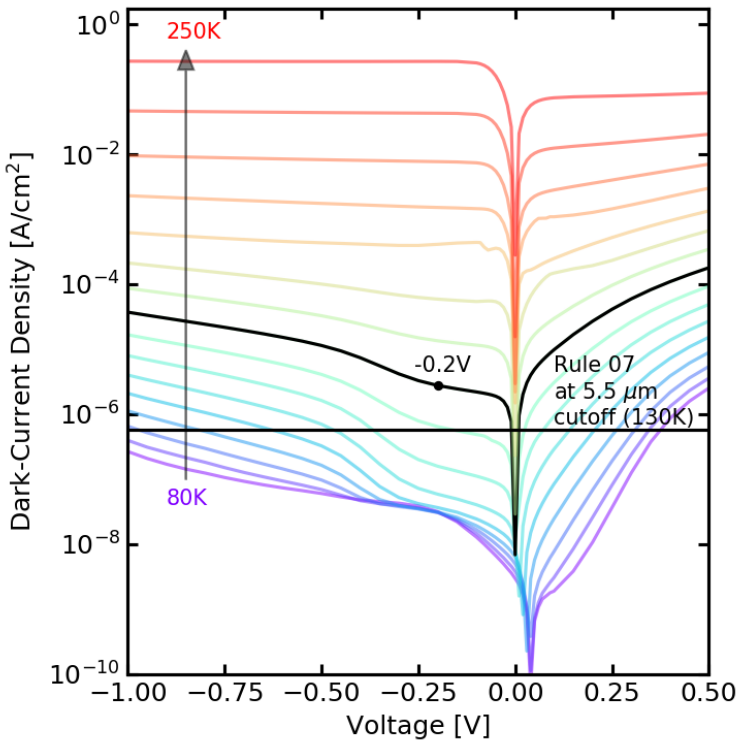

Figure 2: Dark current density shown at temperatures ranging from 80K to 300K for a MWIR photodetector with a 5.5 μm cutoff. Dark current density curve at the detector operating temperature 130K (black curve) with the optimal bias indicated illustrating the variation of the dark current magnitude as the detector bias V_{DET} changes [10].

infrared detector to illustrate how the change of capacitance occurs as a function of voltage bias for an nBn detector.

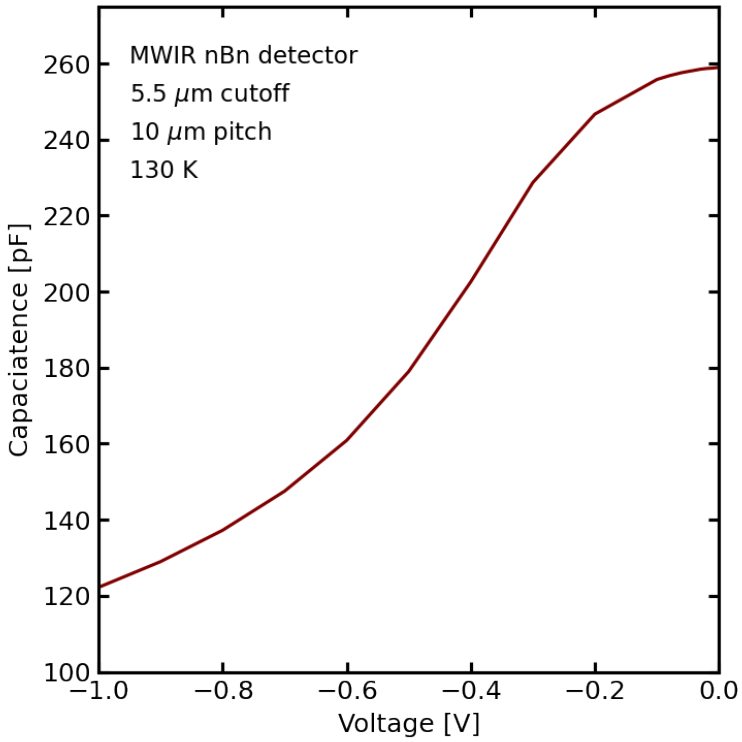

Figure 3: Capacitance density for a MWIR photodetector with a 5.5 μm cutoff shown for a 10 μm pitch device to demonstrate the change of capacitance as a function of voltage bias [10].

2.3 IR EBS Circuit

There are two unique configurations in which the detector may be connected to the photoreceptor, one in which the detector is thermally-connected to the photoreceptor and another in which the detector is not thermally connected to the photoreceptor. The former case is representative of the conventional focal

plane array hybridized on a read-out integrated circuit. At the same time, the latter might be the case in a hypothetical EBS test station where a single-element detector operates in a cryogenic Dewar, with its current outputs routed to the photoreceptor circuit outside of the cryogenic environment. Both scenarios will be analyzed here.

Suppose the 5.5 μm cutoff detector material from [10] is hybridized to a 10 μm pixel pitch read-out integrated circuit with an EBS unit cell utilizing this basic photoreceptor implementation. The resulting EBS camera would operate with both the detector and photoreceptor elements at 130 K. The dark current density data in Fig. 2 indicates that the detector dark current would be 2 pA for this pixel pitch at 130 K. The purple curve in Fig. 2 represents the photoreceptor response at 130 K which shows that under low-light conditions, the 2 pA dark current level will hold the photoreceptor output at about 2 V. Despite the higher dynamic range potential of lower temperature operation, the MWIR detector's dark current ultimately puts a practical limit on the dynamic range of ~ 140 dB.

Alternatively, one may evaluate larger-sized variable-area detector arrays as prototype EBS's using a conventional cryogenic detector test station. The detector output signals (dark current plus photocurrent) are routed to an external circuit implementing the photoreceptor, which may be at any other temperature. In this scenario, device sizes may range from 100 to 1000 μm square mesas, and the detector may be evaluated as a function of temperature to characterize its

performance as a prototype EBS. As seen in Fig. 2, varying the temperature from 80 to 250 K can result in in >7 orders of magnitude change in dark current. For the detector material considered here, the smallest (100 μm side-length) devices would yield dark current levels of 10 pA, while the largest (1000 μm side-length) devices would yield dark current levels of 1 nA. An external circuit implementing the photoreceptor, differencing, and comparator stages could likely be operated at room temperature for basic prototype MWIR EBS characterizations. With increasing temperature, dark current levels would increase, making the smallest devices most useful for probing the high-temperature operational conditions of the detector.

2.4 Subthreshold Conduction

When the gate-source voltage of a MOSFET is lower than the threshold voltage required to fully turn on the transistor, a small amount of current can still pass through the transistor, this is known as subthreshold conduction. This happens due to carriers (electrons or holes) diffusing through the channel region under the influence of a weak gate-source voltage from the source to the drain. The subthreshold conduction rises exponentially with decreasing gate-source voltage and is strongly influenced by temperature and device geometry. The subthreshold swing, which is the change in gate-source voltage necessary to increase the subthreshold current by one decade, is frequently used to describe the subthreshold

current, an important parameter for low-power circuit design.

Both analog and digital designers are particularly interested in the MOSFET sub-threshold regime. This operating region, has a very high transconductance to current ratio, which makes it a particularly productive operating region [17]. A logarithmic function represents the drain current response, hence using weak inversion as the transistor responsible for the logarithmic compression of the signal.

3 Pixel Circuit Operation

3.1 Basic Operation

The standard commercial off the shelf EBS camera uses a pixel unit cell circuit design which consists of three basic stages: (1) photoreceptor; (2) differencing; and (3) comparator in order of the signal path, as shown by the abstracted schematic from Fig. 4. In the photoreceptor stage, the current produced in the photodetector (photocurrent and thermally-generated dark current) is logarithmically compressed and amplified through a MOSFET [3] transistor load operating in weak inversion. In the second stage, the logarithmic photovoltage produced by the first stage is then differenced with respect to the last value that triggered an event. This difference voltage, a signal quantifying the change of illumination or temporal contrast, enters the final comparator stage to be compared to positive and negative contrast threshold values, producing positive or negative events, respectively, at the output of the comparator stage, which is then reported off-chip using address-event representation. In this way, the pixels of the EBS produces data independently of one another, and any given pixel only produces data when the region of the scene it views is evolving [4]. For a static scene, a minimum volume of data is still produced due to background activity, which is a function of the noise due to detector photo- and thermal dark current relative to their median values.

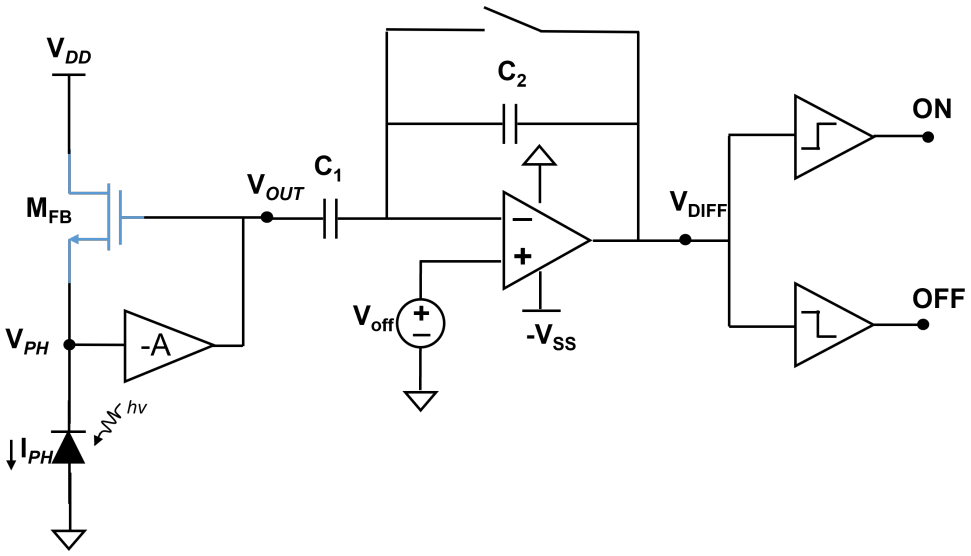

Figure 4: Abstract schematic showing the three basic stages of the EBS pixel circuit; photoreceptor stage with input from the detector and output at V_{OUT}, differencing stage with input from the previous stage and an output of V_{DIFF}, and comprator stage with input from the previous stage and an two outputs (ON and OFF) corresponding to events

Figure 5 plots the basic EBS pixel circuit response at all stages using an expected curve shape for input photocurrent (damped sinusoidal wave). Though the shape of the two curves is similar, the logarithmic compression from the photoreceptor causes the difference in magnitude between Fig.4-a and b, which is then differenced to the previously triggered value resulting in the several peaks with an upper and a lower bands of ON and OFF contrast thresholds. Should the crossing of the horizontal contrast thresholds occur, the signal gets triggered as indicated by the red vertical lines in Fig.4-d.

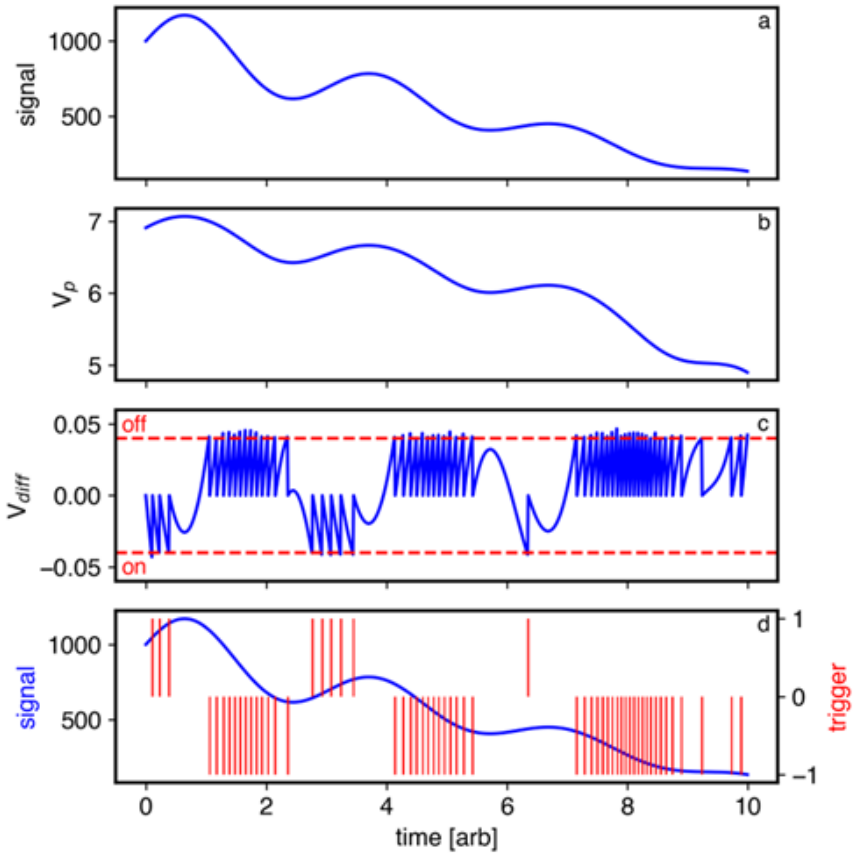

Figure 5: EBS pixel circuit stage response. (a) Example damped sine wave serving as an input to the circuit. (b) logarithmically compressed signal at the output of the first stage. (c) Output voltage from the differential amplifier stage with upper and lower bounds corresponding to ON and OFF levels. (d) Initial signal with its' ON and OFF events (where V_{DIFF}) reached the ON or OFF threshold condition represented by the horizontal dashed lines. Figure used with permission of J. V. Logan

3.2 Detection Stage: Photoreceptor

As mentioned in the previous section (3.1), the photoreceptor is the only stage that receives the signal directly from the photodetector. Additionally, it is in charge of the signal's logarithmic compression, while the subsequent stages are utilized to process the signal as it exits the first stage as shown in Fig.5c and d, making the photoreceptor stage the detection stage. Understanding the limitations of the photoreceptor design allows us to determine the figures of merit of the circuitry for infrared applications and how the design can be modified to better match the requirements.

The remaining sections of this study will focus on finding and optimizing the photorecptor's dynamic range and bandwidth. In addition, determine the limitations of the circuitry caused by the photoreceptor circuit. The EBS pixel circuit implementation with the photoreceptor stage (red stage) shown in Fig. 6 will be analyzed in the following sections.

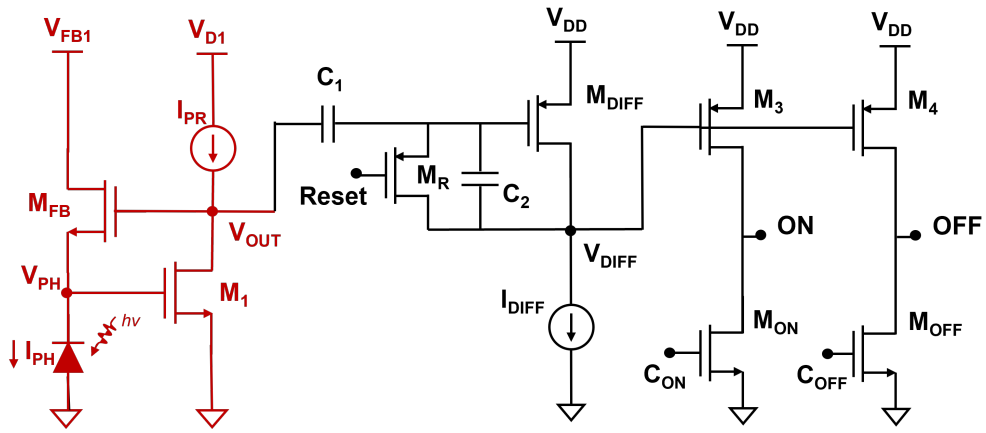

Figure 6: Schematic shows the three fundamental stages of the EBS pixel circuit using a basic implementation

4 DC Analysis

Similar to the human eye, the circuit's first stage is the photoreceptor, the fundamental mechanism for this stage of the circuit is that the current generated by the detector I_{DET}, is converted to voltage V_{DET}, through the high-gain inverting trans-impedance amplifier (shown in Fig 7 With a Photon flux-dependent current from the photodetector as the input and a supply voltage of V_{DD}) An N-type feed-back MOSFET M_{FB} operating in sub-threshold conduction (also referred to as weak inversion) compresses the voltage to the output node V_{OUT} to then serve as input to the differentiating stage.

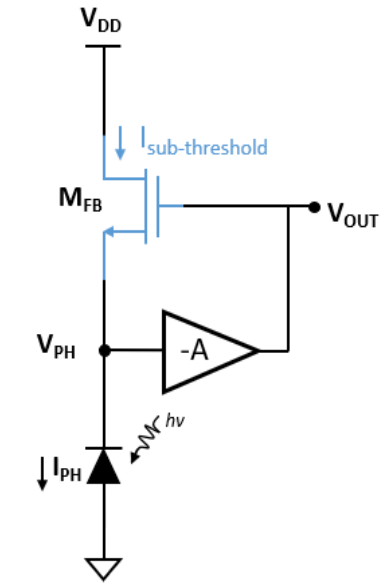

Figure 7: Simplified version of the basic implementation of photoreceptor circuit using transistor M_{FB} operating in subthreshold conduction with a feedback amplifier

Assuming that the M_{FB} transistor branch remains in the subthreshold regime

and the feedback configuration shown in Fig. 7, two expressions can be obtained to represent the relationship between nodal voltages:

$$\begin{aligned} I_{DET} &= I_o \cdot e^{(\frac{V_{OUT}-V_{DET}-V_{T_{M_{FB}}}}{\frac{nkT}{q}})} \\ V_{OUT} &= V_{PH}(-A) \end{aligned} \tag{1}$$

Solving the system of equations in (1), the result becomes

$$V_{OUT}(1+\frac{1}{A}) = \frac{nkT}{q} ln(\frac{I_{PH}}{I_o}) + V_{T_{M_{FB}}} \tag{2}$$

This expression indicates that the output voltage is proportional to the natural log of I_{PH}, which generates the log response for EBS. The equation also shows that for a high amplifier gain (∼infinity), V_{OUT} becomes only dependent on the feedback transistor and its threshold voltage $V_{T_{M_{FB}}}$.

Figure 8 shows the basic implementation of the photoreceptor stage circuit [4] [6], which (for this analysis) uses a 1.1 V voltage supply V_{DD} for the M_1 transistor branch, a 350 mV voltage supply V_{DFB} for the M_{FB} transistor branch, and an ideal current source I_{PR} for tuning the circuit's operating condition. The primary function of the biasing current I_{PR} is to provide an independent means of adjusting the nodal voltage V_{DET}, establishing the photodetector bias condition, and maintaining the M_1 transistor branch in the saturation region.

The fundamental function of the photoreceptor stage in the EBS pixel unit cell circuit is to convert the photodetector current I_{DET} to a logarithmically-

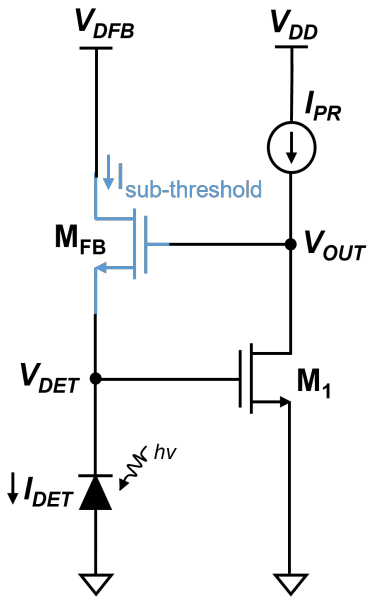

Figure 8: Basic implementation of the stage 1 photoreceptor circuit in an event-based sensing pixel unit cell. When operated with MOSFETs M_1 in saturation and M_{FB} in subthreshold conduction, the photodetector current I_{DET} at detector operating temperature is converted to a logarithmically-compressed voltage at V_{OUT}.

compressed voltage at V_{OUT} [5]. An n-type feedback MOSFET M_{FB} operating in subthreshold conduction acts to convert the current I_{DET} to a logarithmically-compressed signal at the output node V_{OUT}, to then serve as input to the differencing circuit in stage 2 that would follow in the full EBS pixel unit cell.

4.1 Analytical Modeling

4.1.1 Dynamic Range Derivation

This section derives the dynamic range of the photoreceptor circuit, under the conditions that M_{FB} stays in subthreshold conduction and M_1 stays in saturation. For M_{FB} to operate in subthreshold conduction, it must be the case that its gate-source voltage $V_{OUT} - V_{DET}$ is less than its threshold voltage V_{tFB}. Similarly, for M_1 to operate in saturation, it must be the case that the product of its drain-source voltage V_{OUT} and its ideality factor n_1 exceeds its gate-source voltage V_{DET} minus its threshold voltage V_{t1}, and that quantity $V_{DET} - V_{t1}$ is greater than zero [11]. These requirements are expressed in (3).

$$\begin{aligned} V_{OUT} - V_{DET} &< V_{tFB} \\ n_1 V_{OUT} &> V_{DET} - V_{t1} > 0 \end{aligned} \tag{3}$$

Under the assumptions in (3), the circuit in Fig. 8 can be solved analytically. The current I_{PR} passes through the drain-source channel of transistor M_1, governed by (4), which carries a weak dependence on V_{OUT} due to the velocity

saturation factor in square brackets and the channel length modulation factor λ.

$$I_{PR} = \gamma_1 (V_{DET} - V_{t1})^2 (1 + \lambda V_{OUT}) \left[\frac{1}{1 + (\frac{V_{OUT}}{E_c L})} \right] \tag{4}$$

The factor γ_1 contains the effective mobility of the channel μ_{eff1}, gate oxide capacitance C_{ox1}, and the ratio of the channel width to length $\left(\frac{W}{L}\right)_1$ of M_1 as detailed in (5).

$$\gamma_1 = \left(\frac{\mu_{eff1} C_{ox1}}{2 n_1} \right) \left(\frac{W}{L} \right)_1 \tag{5}$$

Rearranging (4) to solve for the photodetector voltage V_{DET} yields (6)

$$V_{DET} = V_{t1} + \sqrt{\frac{I_{PR}}{\gamma_1 (1 + \lambda V_{OUT}) \left[\frac{1}{1 + (\frac{V_{OUT}}{E_c L})} \right]}} \tag{6}$$

Equation 6 indicates that the minimum photodetector bias is defined by the threshold voltage V_{t1} of transistor M_1, and the photodetector bias is tuned using I_{PR}. However, V_{DET} has a small output dependence due to velocity saturation and channel length modulation in transistor M_1 that will have to be evaluated. Given these conditions, V_{t1} should be low enough to enable application of lower photodetector biases via I_{PR}, with the constraint that minimizing V_{t1} will result in enhanced channel length modulation that may introduce undesirable photodetector bias sensitivity to light levels.

To determine the output voltage V_{OUT}, it is noted that the photodetector current I_{DET} passes through the drain-source channel of transistor M_{FB}, governed

by subthreshold conduction in (7). I_{0FB} is a temperature-dependent characteristic current of transistor M_{FB} detailed in (8), which is a function of effective mobility of the channel μ_{effFB}, gate oxide capacitance C_{oxFB}, the ratio of the channel width to length $\left(\frac{W}{L}\right)_{FB}$, the ideality factor n_{FB} of M_{FB}, and the thermal voltage kT.

$$I_{DET} = I_{0FB} \cdot e^{q[(V_{OUT}-V_{DET})-V_{tFB}]/n_{FB}kT} \tag{7}$$

$$I_{0FB} = \mu_{effFB} C_{oxFB} \left(\frac{W}{L}\right)_{FB} (n_{FB} - 1) \left(\frac{kT}{q}\right)^2 \tag{8}$$

Rearranging (7) to solve for V_{OUT} yields (9), which demonstrates the circuit's logarithmic compression of the photodetector signal.

$$V_{OUT} = \frac{n_{FB}kT}{q} \ln\left(\frac{I_{DET}}{I_{0FB}}\right) + V_{DET} + V_{tFB} \tag{9}$$

Comparison of (6) and (9) with the requirements to place M_{FB} in subthreshold and M_1 in saturation in (3) enables definition of the photodetector current conditions over which the circuit operates with logarithmic compression at V_{OUT}. Equation 9 indicates that the quantity $V_{OUT} - V_{DET}$ is less than V_{tFB} for $I_{DET} < I_{0FB}$, thus the characteristic current I_{0FB} of M_{FB} in Equation 8 is the maximum photodetector current for logarithmic compression, beyond which M_{FB} enters saturation and the logarithmic photocurrent response transitions to power law 2. Analysis of the second condition, that $n_1 V_{OUT} > V_{DET} - V_{t1} > 0$ and (7), defines

a minimum photodetector current I_{min} below which V_{OUT} is too low to keep transistor M1 in saturation. (10) provides the range of photodetector current in which the circuit operates with logarithmic compression.

$$\left[I_{min} = I_{0FB} \cdot e^{-q[(n_1-1)V_{DET}+n_1V_{tFB}+V_{t1}]/n_1n_{FB}kT}\right] < I_{DET} < I_{0FB} \tag{10}$$

Together, (9) and (10) define the maximum dynamic range of this photoreceptor configuration. The factor $\frac{n_{FB}kT}{q}$ in (9) multiplied by the natural log of 10 yields the subthreshold swing of transistor M_{FB}. For photodetector currents below I_{0FB}, the log response can be expected to follow this slope until the photodetector current low-limit I_{min} of (10) is reached, at this point, M_1 falls out of saturation, and the circuit turns off. The reciprocal of the exponential factor in the low-limit $\left(e^{q[(n_1-1)V_{DET}+n_1V_{tFB}+V_{t1}]/n_1n_{FB}kT}\right)$ is the maximum potential dynamic range I_{0FB}/I_{min} for this photoreceptor configuration. Given that the quantities $(n_1-1)V_{DET}$ and V_{t1} are small and constrained to establish optimal biasing conditions on the photodetector, the dynamic range at a given temperature is primarily defined by the threshold voltage of the feedback transistor V_{tFB} over $n_1n_{FB}kT$.

4.1.2 Dynamic Range Optimization

The dynamic range equations identified allow optimization of fundamental transistor properties to maximize the dynamic range. The expression for threshold volt-

age V_t is given as a function of the intrinsic carrier concentration n_i and bandgap energy E_g of Si, the substrate acceptor concentration N_A, the base-source voltage V_{BS}, oxide charge density Q_{ox} (qN_{ox}), and the oxide capacitance C_{ox} in (11) [11]. Ideality factor n is a function of the depletion and oxide capacitances and the fast surface state capacitance C_{FS}, and is given as a function of fundamental parameters (depletion width W_D, built-in potential ψ_B, oxide thickness t_{ox}, fast surface state density N_{FS}, and the oxide and silicon permittivity ε_{ox} and ε_{Si}) in (12).

$$V_t = 2\psi_B + \frac{\sqrt{2q\varepsilon_{Si}N_A[2\psi_B - V_{BS}]} - qN_{ox}}{C_{ox}} - \frac{E_g}{2} \tag{11}$$

$$\begin{gathered} \psi_B = \frac{kT}{q} ln\left(\frac{N_A}{n_i}\right) \\ C_{dep} = \frac{\varepsilon_{Si}}{W_D} = \sqrt{\frac{qN_A\varepsilon_{Si}}{2\psi_B}}, C_{ox} = \frac{\varepsilon_{ox}}{t_{ox}}, C_{SF} = q(N_{SF}) \\ n = 1 + \frac{C_{dep}}{C_{ox}} + \frac{C_{FS}}{C_{ox}} = 1 + \frac{\varepsilon_{ox}}{t_{ox}}\left[\sqrt{\frac{qN_A\varepsilon_{Si}}{\frac{2kT}{q} ln\left(\frac{N_A}{n_i}\right)}} + qN_{FS}\right] \end{gathered} \tag{12}$$

Given that there are several common factors defining threshold voltage V_t and ideality factor n, it is important to optimize the selection of these parameters to maximize the dynamic range for the photodetector to be used. For example, (9) may lead one to believe that dynamic range can be maximized by decreasing the substrate acceptor concentration N_A of transistor M_{FB}, as that reduces its ideality factor n_{FB}, reducing M_{FB}'s subthreshold swing and increasing the degree

of logarithmic compression as a result. However, decreasing acceptor concentration also reduces the threshold voltage, increasing the minimum current I_{min} and ultimately reducing the dynamic range.

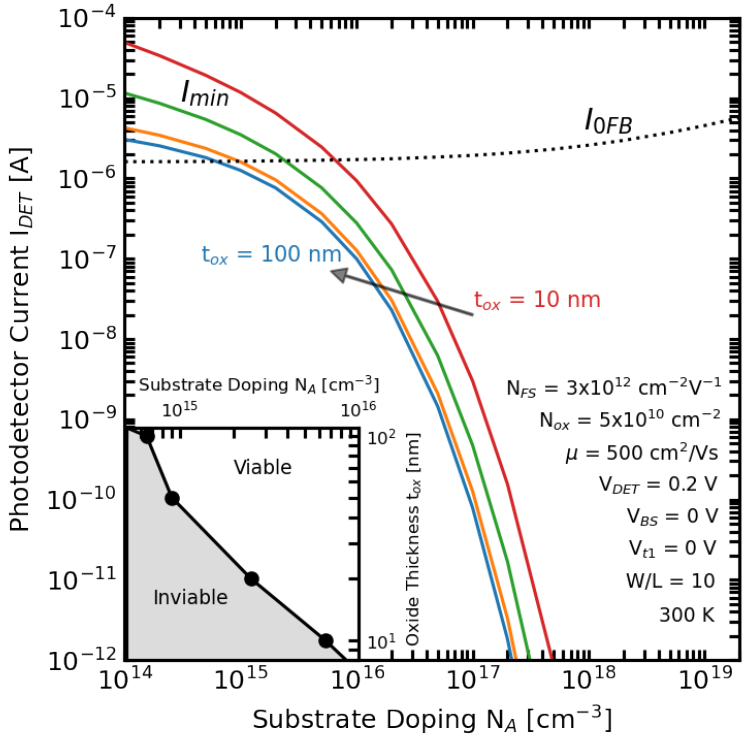

Figure 9: Photodetector current I_{DET} as a function of substrate doping concentration N_A, showing the maximum (I_{0FB}, dotted line) and minimum (I_{min}, solid curves) photodetector currents for log-response circuit operation. Inset shows the region of viable designs as a function of oxide thickness and substrate doping in the feedback transistor.

Figure 9 plots the maximum and minimum photodetector currents for log response, I_{0FB} and I_{min} defined by (8) and (10), as a function of acceptor concentration N_A on the horizontal axis, for various values of oxide thickness t_{ox}. There is no oxide thickness dependence in I_{0FB} (dotted line), as the factor of C_{oxFB} in (8)

is cancelled by the factor $(n_{FB}-1) = C_{dep}/C_{ox}$. Increasing N_A therefore increases I_{0FB} by increasing the depletion capacitance C_{dep}, and reduces the minimum photodetector current I_{min} for all oxide thicknesses (solid curves) by increasing the threshold voltage. For a given oxide thickness, the intersection of the dotted and solid curves identifies the minimum doping level below which the threshold voltage is too low for the circuit to function ($I_{min} > I_{0FB}$), which is shown in the inset. To design this circuit for operation with a particular photodetector element, one would identify the minimum photodetector current expected for the application and pixel size, and then select the oxide thickness curve that provides sufficient dynamic range to achieve the maximum expected photodetector current. The transistor geometry parameter $\frac{W}{L}$ can provide some additional flexibility to tune the dynamic range within the geometric constraints of the pixel dimension, as can the substrate bias V_{BS} to further tune the feedback transistor's threshold voltage or account for uncertainty in oxide charge density Q_{ox}.

4.2 Voltage Transfer Characteristics

The photodetector is simulated with an ideal current source producing current I_{DET} to simulate the photodetector current. The magnitude of I_{DET} would represent the sum of the 5.5 μm cutoff photodetector's photocurrent and thermally-generated dark current at the operating bias V_{DET}. The simulations presented in the following sections use a level three T-Spice built-in transistor model [8], which

includes the equations needed to account for all transistors' regions of operation; sub-threshold conduction, linear, and saturation, with the minimum conductance global variable G_{min} set to $1 \times 10^{-20}\ \Omega^{-1}$.

4.2.1 M_1 Transistor Branch

For discrete MOSFET amplifiers, it is crucial to keep the active load I_{PR} within limits such that the transistor's operation region remains in saturation. Though this means that there is a limitation on what the photodetector can be biased at, keeping M_1 in saturation will allow the entire signal to be amplified without any clipping, as demonstrated in Fig. 10-b; which shows the regions of operation for M_1 values of V_{OUT} as a function of V_{DET}. Points A and B in Fig. 10-b represent the bounds for the saturation region, implying that the photo-detector biasing V_{DET} should not exceed $\sim 0.45V$ to avoid the transition to the linear region. The bounds have a slight dependence on I_{PR}, where, as the biasing current I_{PR} increases, the slope between the two points becomes steeper.

Since the threshold voltage for M_1 is zero, there isn't a cut-off region ($V_{GS} < V_{T_{M_1}}$) and the transistor is always on, this is shown by Fig.10; evidently for all V_{DET} values in Fig.10-a transition into saturation for very low Drain-Source V_{OUT} after operating in the linear region as demonstrated by the gray shaded area on the figure.

Figure 10 A also reveals a Channel Length Modulation (CLM) effect caused

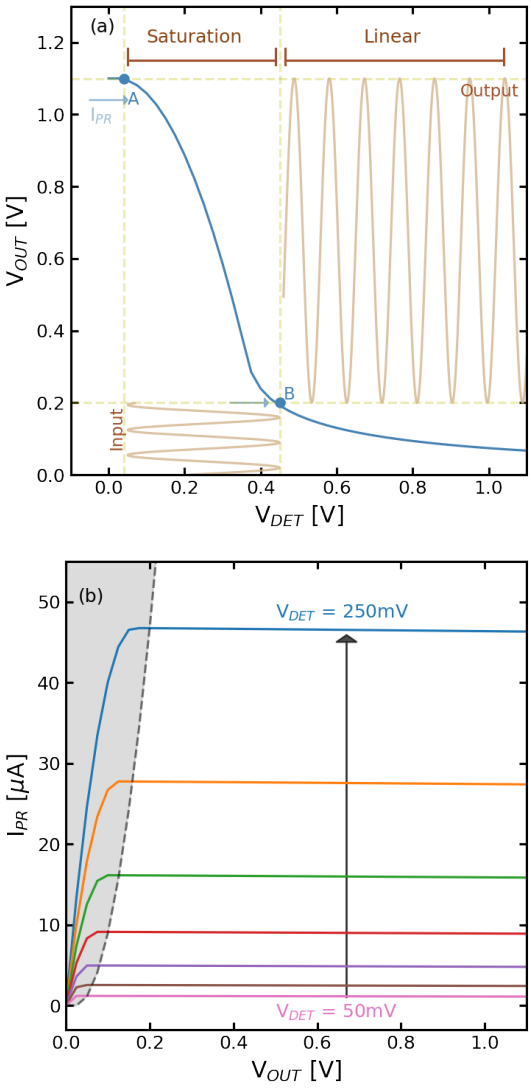

Figure 10: M_1 biasing bounds (a) Drain-Source voltages V_{OUT} as a function of Gate-Source voltages V_{DET} with an example sinusoidal wave input and its' corresponding amplified output, without signal clipping. (b) Biasing current I_{PR} as a function of the Drain-Source voltage V_{OUT} shown at various Gate-Source V_{DET} voltages

by the shortening of the inverted channel length, shown as the increasing slopes as V_{GS} increases; this effect reduces the small-signal amplifier gain by introducing an additional resistance.

4.2.2 M_{FB} Transistor Branch

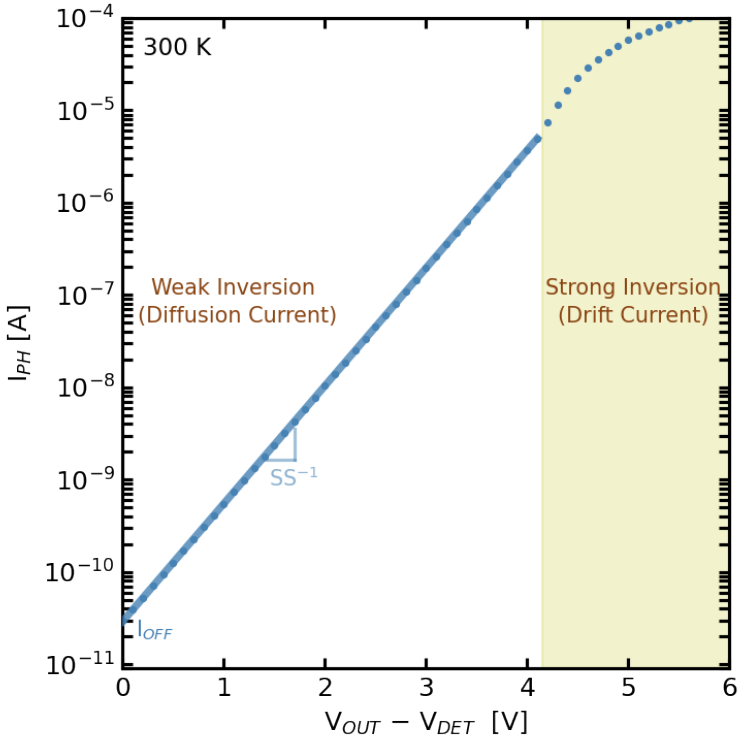

Figure 11: M_{FB} drain current I_{PH} as a function of Gate-Source voltage with a fit at the weak inversion side demonstrating sub-threshold swing [S] $\frac{1}{m}$, and Off current as the y-intercept of the fit. The tan region represents the turn-on point of the transistor, where its' current mechanism changes from diffusion to drift current.

Sub-threshold swing is a crucial metric for determining the transistor's weak inversion behavior. This value can be quantified in $[\frac{Volts}{Decade}]$ as the inverse of the

rate of change of the drain current I_{PH} before M_{FB} moves into strong inversion as shown in Fig. 11. The figure also implies that the Gate-Source voltage can not exceed $\sim 4.1V$, to remain in the logarithmic regime.

4.2.3 Nodal Voltages

As (6) indicates that a low threshold voltage for M_1 <0.2 V is needed to provide photodetector bias tunability through photoreceptor branch current I_{PR}, the circuit is modeled with an oxide thickness of 15 nm and acceptor concentration of $1.5 \times 10^{16}\ cm^{-3}$ for transistor M_1 to provide a room temperature threshold voltage of 8.5 mV. The inset to Fig. 12a plots the photodetector voltage bias V_{DET} as a function of the circuit tuning current I_{PR} (drain-source current of M_1) at 300 K, with the 0.2 V operating point indicated with the vertical arrow at I_{PR} = 45 μA.

Given that the differential conductivity of the dark current at the -0.2 V operating point is non-zero and the detector bias V_{DET} carries an output-dependence V_{OUT} in (6), V_{DET}'s sensitivity to I_{DET} could be a source of positive feedback that destabilizes the photoreceptor. The main body of Fig. 12-a plots V_{DET} at I_{PR} = 45 μA, as a function of photodetector current I_{DET} and temperature to evaluate the stability of the operating point. The dotted sections of the curves at the lowest current levels show V_{DET}'s behavior when the subthreshold conduction channel of the feedback transistor M_{FB} is extinguished. The photoreceptor is not

operational in this regime for reasons elaborated in Fig. 12b discussion that follows. In the functional operational regime indicated by solid curves in Fig. 12a, the photodetector bias V_{DET} is 0.2 V at 300 K and has a temperature-dependence through the threshold voltage of V_{t1}. This implies that a change in the operating temperature of the unit cell circuit will necessitate an adjustment to I_{PR}. For any given temperature in the functional operational regime (solid curves), V_{DET} varies by less than $0.05\frac{\%}{decade}$ over several orders of magnitude in I_{DET}. This $0.05\frac{\%}{decade}$ sensitivity is much less than the rate of change of dark current with bias, and affirms that V_{DET} is not likely to be disturbed by random noise fluctuations in the dark current. This indicates that channel length modulation and velocity saturation effects in M_1 are not substantial, and the denominator in the square-root term in (6) can be approximated as γ_1.

As the properties of M_{FB} play a significant role in defining the logarithmic response, Fig. 9 is used as a guide in the selection of this transistor to achieve a suitable dynamic range between I_{min} and I_{0FB}. Modeling M_{FB} with oxide thickness of 70 nm, acceptor concentration of $1.5 \times 10^{17} cm^{-3}$ and M_1 as described above, Fig. 12b plots the output voltage V_{OUT} as a function of the photodetector current I_{DET} from 300 to 77 K. Here again, the solid sections of curves represent the circuit behavior in the functional operational regime. In contrast, the dotted curves show the behavior when the subthreshold conduction channel of the feedback transistor M_{FB} is extinguished (low I_{DET}) or goes into strong inver-

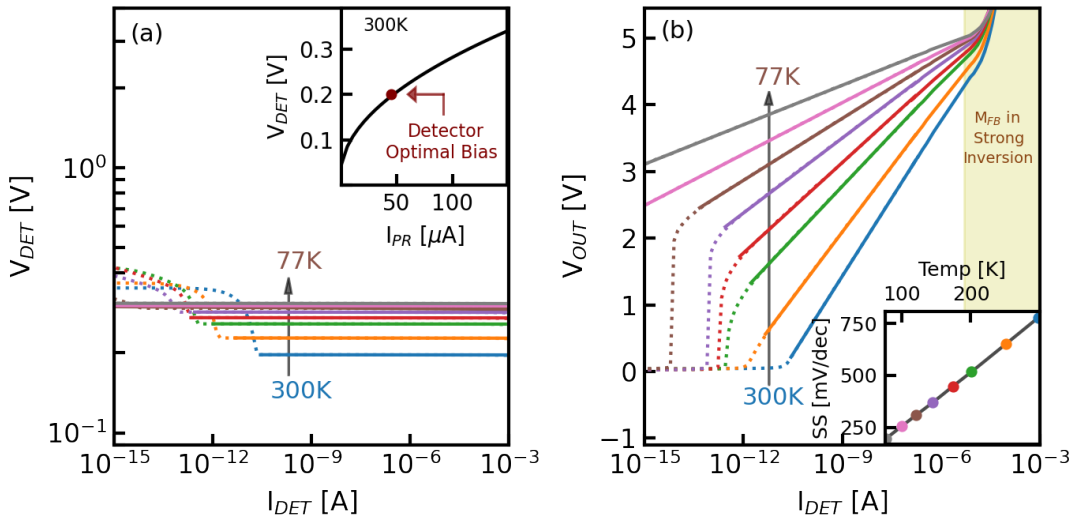

Figure 12: (a) Inset plots the photodetector bias voltage V_{DET} as a function of biasing currents I_{PR}, with optimal detector reverse bias voltage of 0.2 V indicated. Main body of the figure plots photodetector bias voltage V_{DET} at this I_{PR}, as a function of detector current I_{DET} and decreasing temperature from 300 to 77 K; (b) Output voltage V_{OUT} as a function of detector current I_{DET}, for the specific I_{PR} which establishes the optimal 0.2 V operating bias on V_{DET}. The tan shaded area shows the change of operation of the feedback transistor M_{FB} from weak inversion to strong inversion. Inset plots the subthreshold swing corresponding to each output voltage temperature V_{OUT}.

sion (high I_{DET}). Comparing the solid curves in Fig. 12b to (9), it can be seen that the current I_{DET} obeys the subthreshold regime expectation in (9) over five orders of magnitude in I_{DET} resulting in a dynamic range of at least 100dB at room temperature, increasing with a temperature-dependent characteristic voltage of (n_{FB} kT)/q (n_{FB} = 5.52 at room temperature) while V_{OUT}-V_{DET}<V_{tFB} (unshaded region).

As $V_{OUT}-V_{DET}$ approaches V_{tFB}, I_{DET} converges on I_{0FB} and M_{FB} transitions into strong inversion, with V_{OUT} varying as power law half with increasing I_{DET} (shaded region). The circuit would be functional here, but would not provide logarithmic compression of the photocurrent. In the regime of log response (unshaded region), the subthreshold swing is evaluated along the highlighted section of each curve and plotted as a function of temperature in the inset to Fig. 9. This shows the higher degree of logarithmic compression offered by the lower subthreshold swing of lower operating temperature operation; however, it can be seen that this does not necessarily result in a substantially greater dynamic range (see the main body of Fig. 9). As V_{OUT} decreases with decreasing photodetector current I_{DET}, at room temperature (blue curve), the circuit turns off as expected when the current reaches the minimum circuit current I_{min}. However, at lower temperatures, the photoreceptor is found to turn off prematurely (dotted curve sections at low I_{DET}). Analysis of the currents going into and out of M_{FB} indicates that the subthreshold conduction channel closes when I_{DET} falls below the reverse satu-

ration leakage current conducting between the substrate-source junction of M_{FB}. At this point the subthreshold conduction channel of M_{FB} is extinguished as detector current conducts across the substrate-source junction, initiating a collapse of V_{OUT} that causes M_1 to exit the saturation regime.

While Fig. 9, derived from the analytical analysis of (10 - 12), had indicated that increasing acceptor concentration N_A would increase dynamic range by decreasing I_{min}, the T spice simulations here show that the dynamic range is practically limited by the reverse saturation current of the substrate-source junction of M_{FB} as shown in Fig. 13 which plots the drain and bulk currents as a function of I_{DET}. It is noted that as the drain current of M_{FB} (blue curve) crosses zero, the bulk current of M_{FB} (orange curve) remains positive, driving the amplifier to exit the saturation region. The ratio of the drain current to I_{DET} plotted in the inset of Fig. 13 demonstrates the point where the detection in the photoreceptor becomes circuit limited in place of noise equivalent irradiance.

The reverse junction leakage or substrate current expression can be represented using the cross-sectional area A, intrinsic carrier concentration n_i, acceptor concentration N_A, donor concentration N_D, electrons and holes diffusion coefficients D_n and D_p, and the lifetimes τ_n and τ_n. For the n+p junction formed here, this reduces to just the component of reverse saturation current generated on the substrate side of the junction as shown in (13).

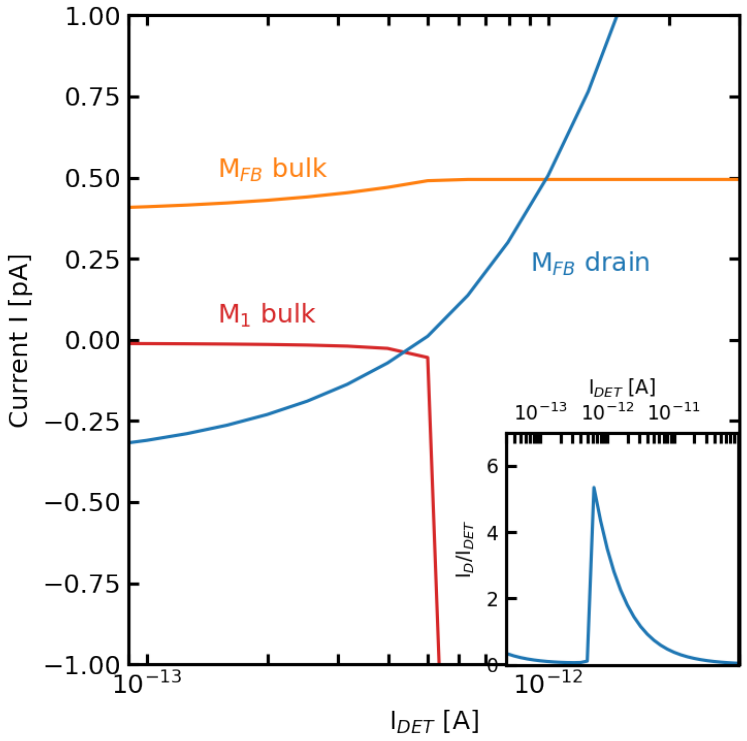

Figure 13: M_{FB} drain and bulk currents with M1 bulk current as a function of detector current I_{DET} simulated at 77 K. Inset plots the corresponding ratio of the drain current to detector current as a function of detector current I_{DET}.

$$I_s = qAn_i^2(\frac{1}{N_D}\sqrt{\frac{D_p}{\tau_p}} + \frac{1}{N_A}\sqrt{\frac{D_n}{\tau_n}}) \cong \frac{qAn_i^2}{N_A}\sqrt{\frac{D_n}{\tau_n}} \tag{13}$$

These results indicate that Fig. 12 would remain valid while $I_{min}>I_s$, but that I_s imposes a practical limitation to the dynamic range. Increasing N_A continues to reduce the limiting current I_s, but the dynamic range does not increase at the rate that it would be predicted to in Fig. 9 or (10).

The simulation was found to include the substrate current by using the principle of Kircoff's current law [14], defined as the sum of currents leaving the node to be zero, which leads to the calculation of a reverse current that is drawn from the substrate contact. This charge is deducted from the detector current entering the source contact, resulting in the premature extinction of the drain-source channel when the detector current drops below the reverse current. The issue with this approach is that the reverse leakage current is generated by thermal processes and should be incorporated as a thermal generation term into the node, rather than being derived from the source contact current. The sudden drop of voltage observed in Fig. 12 is an artifact of the transistor model's inadequate sophistication. To mitigate the issue, the circuit was simulated with the bulk terminal open so that the current dissipates when entering that terminal, thus only accounting for the reverse saturation current from the bulk as shown in Fig. 14. Here in

Fig. 14-b, the output voltage V_{OUT} continues to decrease until the circuit turns off for all simulated tempreture.

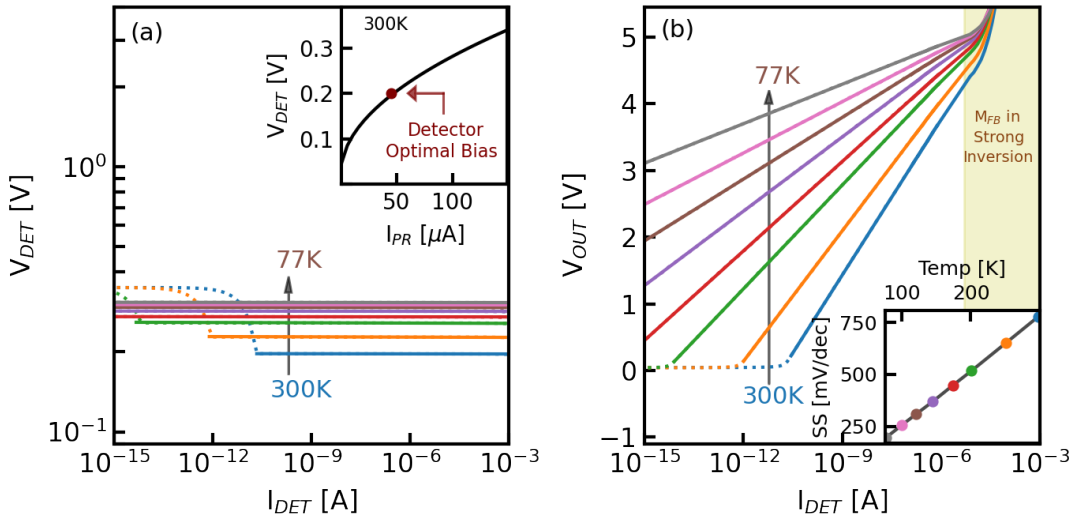

Figure 14: (a) Inset plots the photodetector bias voltage V_{DET} as a function of biasing currents I_{PR}, with the optimal detector reverse bias voltage of 0.2 V indicated. Main body of the figure plots photodetector bias voltage V_{DET} at this I_{PR}, as a function of detector current I_{DET} and decreasing temperature from 300 to 77 K; (b) Corrected Output voltage V_{OUT} as a function of detector current I_{DET}, for the specific I_{PR} which establishes the optimal 0.2 V operating bias on V_{DET}. The tan-shaded area shows the change of operation of the feedback transistor M_{FB} from weak inversion to strong inversion. Inset plots the subthreshold swing corresponding to each temperature of the output voltage V_{OUT}.

4.3 Dynamic Range

Figure 15 plots the subthreshold swing (blue curve) and dynamic range (red curve) simulated in T-SPICE as a function of substrate acceptor concentration N_A on the horizontal axis to show the realistic expectation for dynamic range for this

implementation of the photoreceptor at room temperature. Though (12) shows that increasing N_A reduces the subthreshold swing, which should in-turn increase the dynamic range, the change in N_A has simultaneously reduced the threshold voltage. The T-SPICE simulation results in Fig. 15 affirm that the feedback transistor's threshold voltage is the dynamic range's main driver. Dynamic range could be expected to continue to increase with increasing acceptor concentration until the onset of tunneling breakdown of the junction, which is not simulated here. Dynamic range limits were not affected by the correction made to the simulation code explained in the previous section since the simulated case here is shown for room temperature.

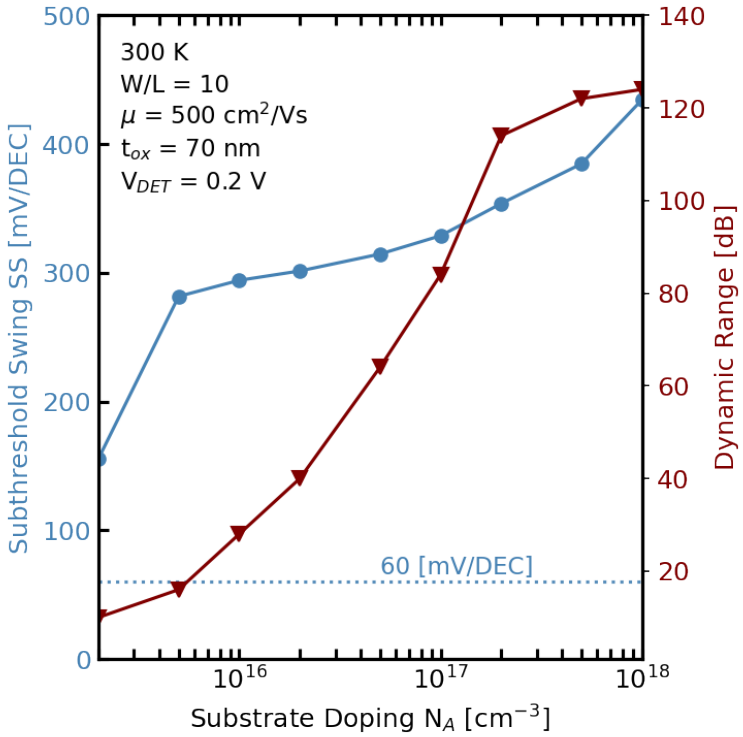

Figure 15: Subthreshold swing (blue curve) and dynamic range (red curve) as a function of substrate doping concentration N_A, shown in reference to the room temperature thermal limit swing of 60 mV/decade.

5 AC Analysis

5.1 Small-signal Gain

5.1.1 Model Configuration

Though the signal gain was discussed in section 4.2.2, to understand the non-linear behavior of the circuit, the small signal approximation can be used to find some circuit properties such as gain by assuming that the response is linear for a very small region.

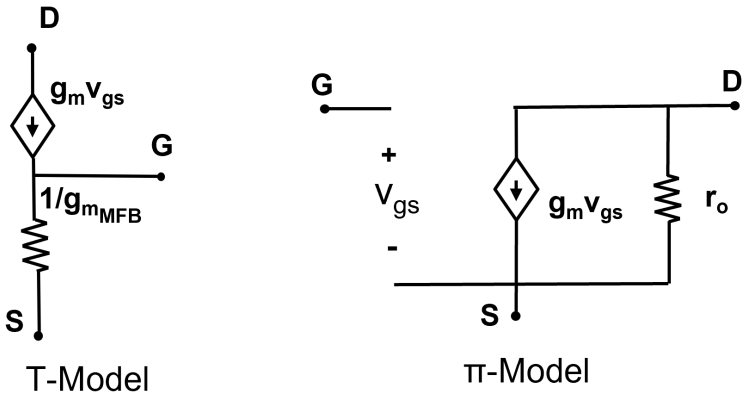

Figure 16: Transistor small-signal π and T models

Using the π and T small-signal transistor models presented in Figure 16 as the basis of creating the small-signal model for the photoreceptor circuit. For simplicity, assuming that M_{FB} is a block and applying it to the π-Model with respect to the transistor terminals as demonstrated in Fig. 17.

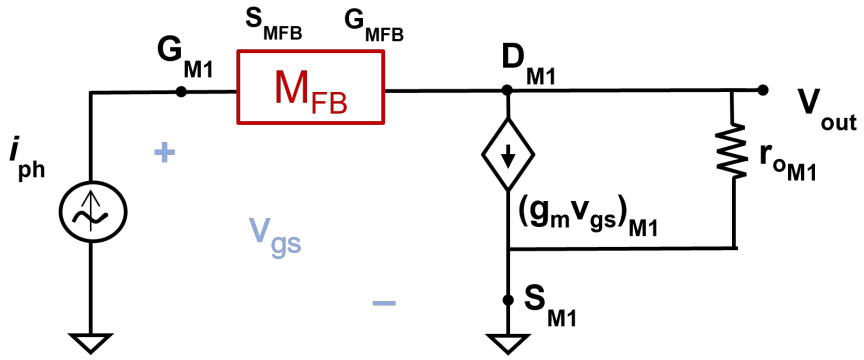

Figure 17: π transistor small-signal model representing M_1 with M_{FB} transistor represented as a block

Rotate and flip M_{FB} to match the terminals (drain to drain, source to source, and gate to gate) so that the transistor model fits within Fig. 17.

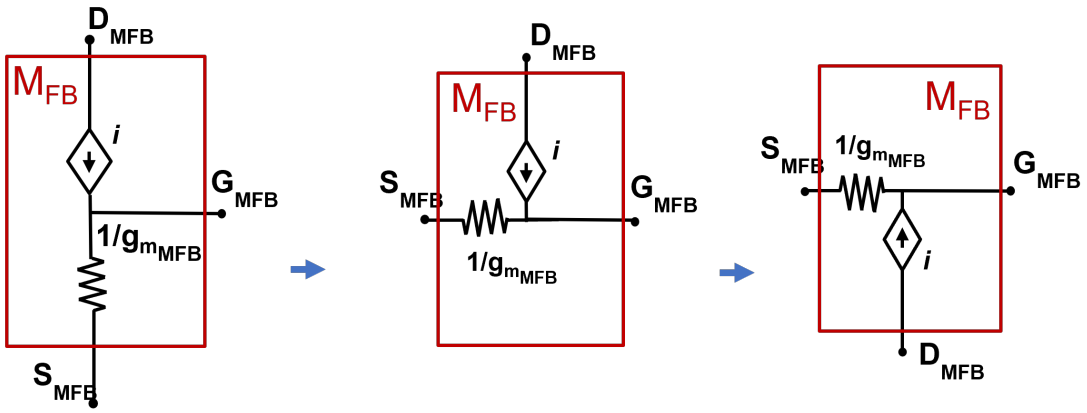

Figure 18: T transistor small-signal model representing M_{FB} rotated and altered so that it fits within Fig. 17

Inserting M_{FB} block into the M_1 π-Model results into a circuit that represents the small signal equivalent of the photoreceptor circuit (from Fig. 8) illustrated in the schematic below (Fig. 19)

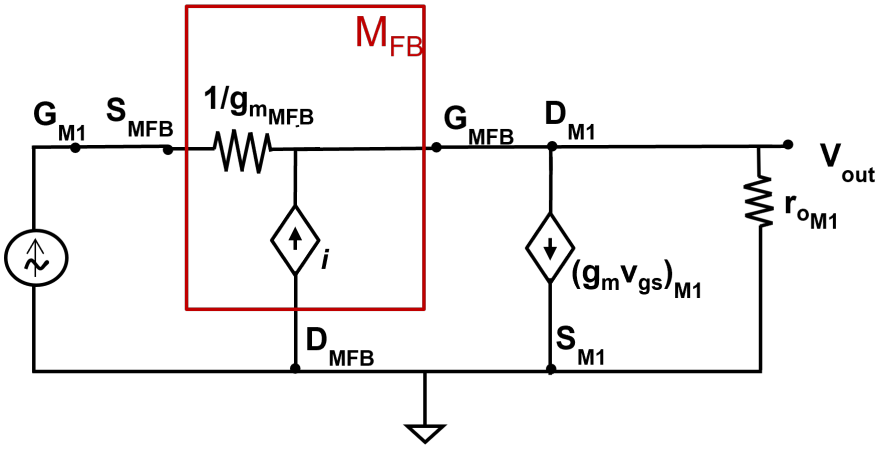

Figure 19: photoreceptor small-signal model

5.1.2 Model Analysis

The model created in Section 5.1.1 can be used to simplify the small-signal circuit gain analysis, through the use of Kirchhoff's current law (KCL), Applying KCL to Fig. 20 results into the system of equations presented in (14).

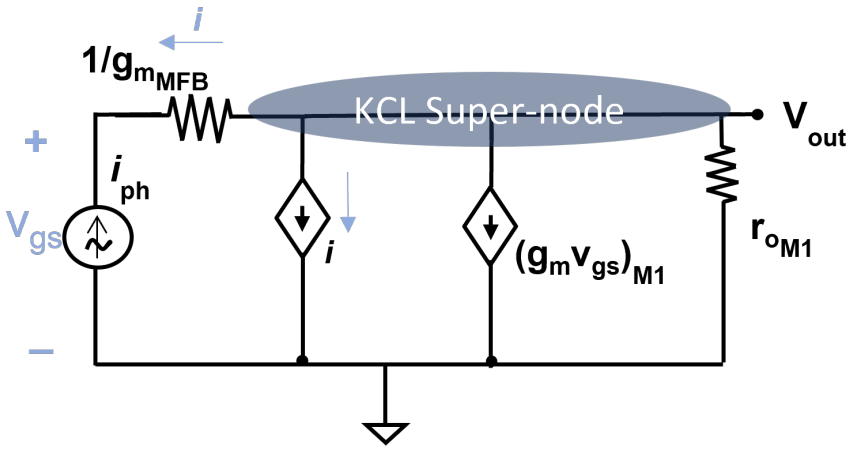

Figure 20: photoreceptor small-signal model with a super node noted to find all the currents leaving the node

$$
\begin{aligned}
i &= i_{DET} \\
v_{OUT} &= v_{gs} + \frac{i_{DET}}{g_{mfb}} \\
v_{OUT} &= -g_{m1} v_{gs}
\end{aligned}
\tag{14}
$$

solving for the system of equations yields the small signal gain

$$
\frac{v_{OUT}}{i_{DET}} = \frac{-g_{m1} r_o}{g_{mfb}(1 + g_{m1} r_o)} = A \tag{15}
$$

Where r_o is $\frac{V_A}{I_D}$, accounts for the channel length modulation factor λ through the inverse of early voltage V_A, g_{m1} represents the transconductance for the M_1 transistor branch (presented in (16)).

$$
g_{m1} = \frac{2 I_{PR}}{V_{DET} - V_{t1}} \tag{16}
$$

Since M_{FB} operates in subthreshold conduction the transconductance, g_{m1} equation in (16) only applies to M_1, the equation can be derived using the definition of transconductance and the subthreshold drain current expression presented in (7), the transconductance equation for the subthreshold region can be found in (17).

$$
\begin{aligned}
g_{mfb} &= \frac{\mathrm{d}I_D}{\mathrm{d}V_{GS}} = \frac{\mathrm{d}}{\mathrm{d}V_{GS}} (I_{0FB} \cdot e^{q[(V_{OUT} - V_{DET}) - V_{tFB}]/n_{FB} kT}) \\
&= \frac{q}{n_{fb} KT} I_{0FB} \cdot e^{q[(V_{OUT} - V_{DET}) - V_{tFB}]/n_{FB} kT}
\end{aligned}
\tag{17}
$$

Equations 15 through 17 indicate that the gain can be altered by varying the drain output resistance parameter r_o through channel length modulation λ and the transistor channel length L.

5.2 Parasitic Capacitance

5.2.1 Transistor Parasitic Capacitance

In this section, the detector parasitic capacitance is assumed to be zero. To assess the AC response of a circuit, in purpose of finding the bandwidth; in AC response, DC current sources cause open circuit in place of the source, while DC voltage sources become short circuit in place of the source.

Transistor parasitic capacitance is mainly affected by miller capacitor any capacitor connected between two nodes (one end isn't grounded), must be turned into two equivalent capacitors (Red capacitors represent the millered capacitors)

Figure 21-(a), $C_{GS_{MFB}}$ and $C_{GD_{M1}}$ are in parallel , here they can be combined into one capacitor $(C_{GS_{MFB}} + C_{GD_{M1}})$, from the definition of miller capacitors, Fig.21-(b) capacitor can be turned into two equivalent capacitors, represented by C_1 and C_2 shown in equation 18, since the capacitor $(C_{GS_{MFB}} + C_{GD_{M1}})$ is connected to two nodes.

$$\begin{aligned} C_1 &= (C_{GS_{MFB}} + C_{GD_{M1}})\,[1 - A] \\ C_2 &= (C_{GS_{MFB}} + C_{GD_{M1}})\left[1 - \left(\frac{1}{A}\right)\right] \end{aligned} \tag{18}$$

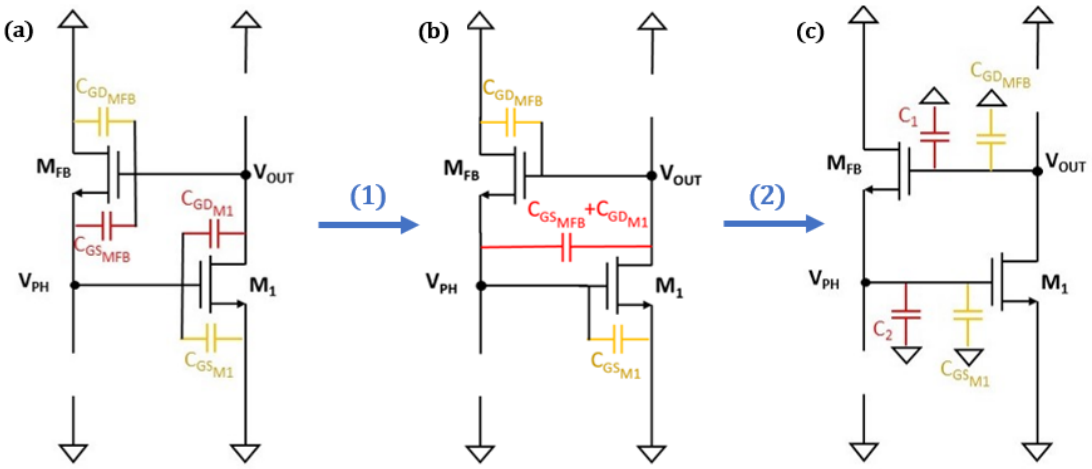

Figure 21: Photoreceptor circuit parasitic gate-source and gate-drain capacitors for the two transistor branches (1) $C_{GS_{MFB}}$ and $C_{GD_{M1}}$ are in parallel so they can be combined into one capacitor (red capacitor)(2) Since the equivalent capacitor (red capacitor) is connected to two nodes, it is turned into two equivalent capacitors, C1 and C2.

After the second transition (2) shown in the schematic in Fig. 21-2, the millered and remaining parasitic capacitors can be grouped into two capacitors because they are connected in parallel since the number of poles is dependent on the number of equivalent capacitors, the two groups represent two pole capacitance shown in (19).

$$C_{pole1} = C_{GS_{M1}} + C_2$$
$$C_{pole2} = C_{GD_{MFB}} + C_1 \tag{19}$$

Using the pole capacitance equations in (19) and the RC network frequency

approximation $\frac{1}{2\pi C_x R_{eq}}$ can provide a quick estimate for the frequency at the poles, the lower pole frequency corresponds to the cut-off point for the bandwidth.

$$\begin{aligned} f_{p_1} &= \frac{1}{2\pi(C_{pole1})(\frac{1}{g_{mfb}}||r_{om1})} \\ f_{p_2} &= \frac{1}{2\pi(C_{pole2})(r_{omfb})} \end{aligned} \tag{20}$$

From (20), it is noted that bandwidth can be controlled by determining the dominant pole (causing the earlier cutoff) and ensuring the use of a transistor with a smaller magnitude of capacitance corresponding to the dominant pole capacitor.

5.2.2 Detector and Transistor Parasitic Capacitance

In this section, the detector capacitance is accounted for as part of the parasitic capacitance of the circuit. While C_1 and C_2 remain the same as (18), the pole capacitance is now different as shown in (21); since the capacitance associated with each pole changes due to the addition of the detector capacitance, represented by C_{part}.

$$\begin{aligned} C_{pole1} =& C_{GS_{M1}} + C_2 + C_{part} \\ C_{pole2} =& \ C_{GD_{MFB}} + C_1 \end{aligned} \tag{21}$$

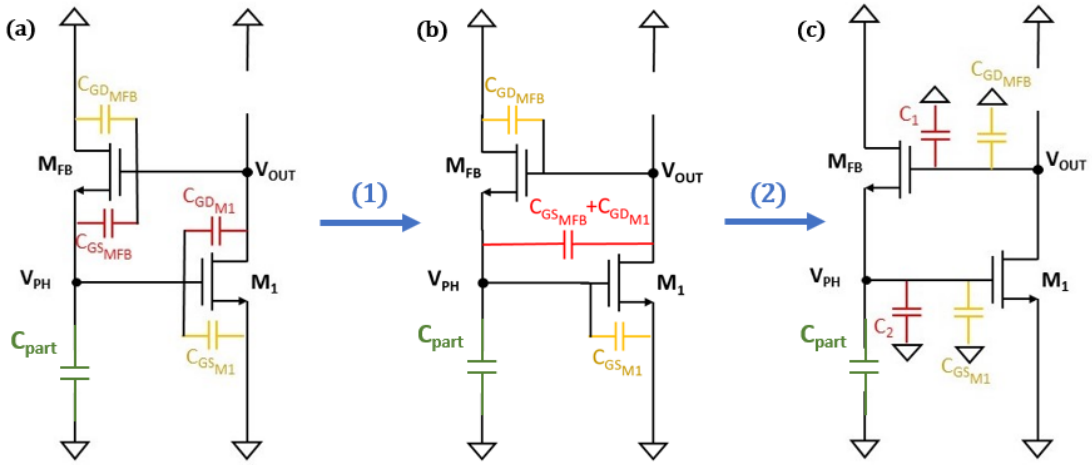

Figure 22: Photoreceptor circuit parasitic gate-source, gate-drain capacitors for the two transistor branches, and the detector capacitance (1) $C_{GS_{MFB}}$ and $C_{GD_{M1}}$ are in parallel so they can be combined into one capacitor (red capacitor)(2) Since the equivalent capacitor (red capacitor) is connected to two nodes, it is turned into two equivalent capacitors, C1 and C2.

5.3 Bandwidth

5.3.1 Transfer function

Using the expressions derived in Sections 5.1.2 and 5.2, the transfer function can be derived using the generic transfer function presented in (22)

$$H(s) = \frac{V_{OUT}}{I_{DET}} = \frac{A}{(s+\omega_c)^2} = \frac{A}{s^2 + 2\omega_c s + \omega_c^2} \tag{22}$$

Where ω_c is the angular cutoff frequency; $2\pi f_c$, and the small signal midband gain A.

Using the transfer function from (22) and assuming that the first pole is the dominant one (with $\omega = 2.3$ radians) with a gain of 135dB; Fig. 23 was obtained.

The figure demonstrates a cutoff frequency of 6.1 kHz indicated by the dashed vertical line found as 70 % of the mid-band gain, which is approximately 500 Hz different than the cutoff discussed in Section 5.3.2.

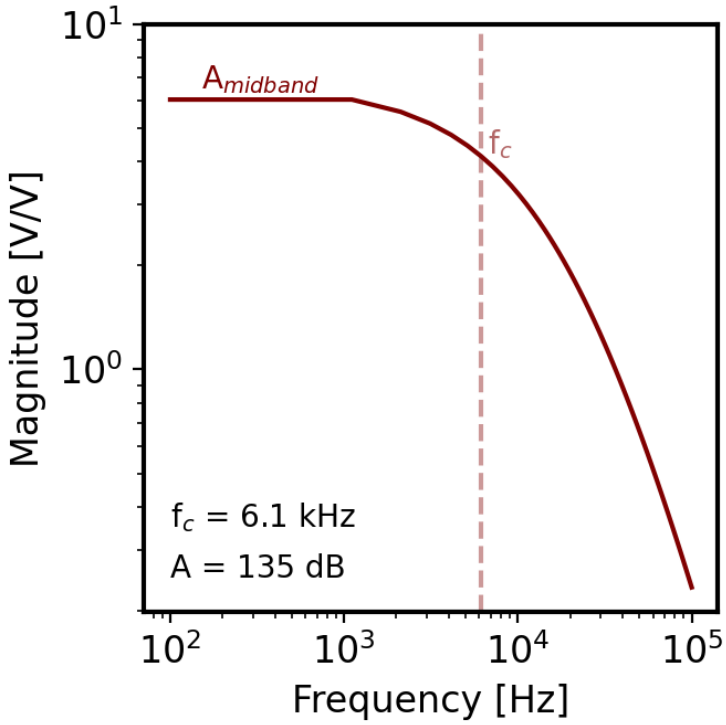

Figure 23: Transfer Function Bode Plot from the derived equations resulting in a cutoff frequency of 6.1kHz, and a midband gain of 135 dB.

5.3.2 Dependence on Circuit Parameters

Since some input sources are constant and some circuit parameters will be variable, such as input illumination, the effect of those changes must be well studied to understand the impact it might have, and how to mitigate it.

Figure 24-a plots the frequency cutoff points for various detector currents

ranging from 100 pA to 300 nA with vertical lines representing the maximum gain minus 3 dB cutoff frequency. The expected photocurrent magnitudes of an nBn MWIR detector for photon flux of ϕ_p = 4.7 x 10^{13} $\frac{photons}{cm^2 s}$ are shown in Fig. 24-b, which plots the cut-off frequencies as a function of input current. This dependence is very important because when designing a specific detector, its photocurrent range must be within a specific limit, depending on the bandwidth requirements for the test case.

The bandwidth exhibits a strong dependence on the input detector, corresponding to the photon flux-dependent photocurrent and noise dark current, however, Fig. 25 shows minimal dependence on detector bias on bandwidth, meaning that through the dark current is not constant for the detector.

With the optimized transistor parameters, a bandwidth of approximately 5kHz can be achieved in the basic photoreceptor circuit configuration, which is 2kHz more than the 3kHz bandwidth reported in the literature.

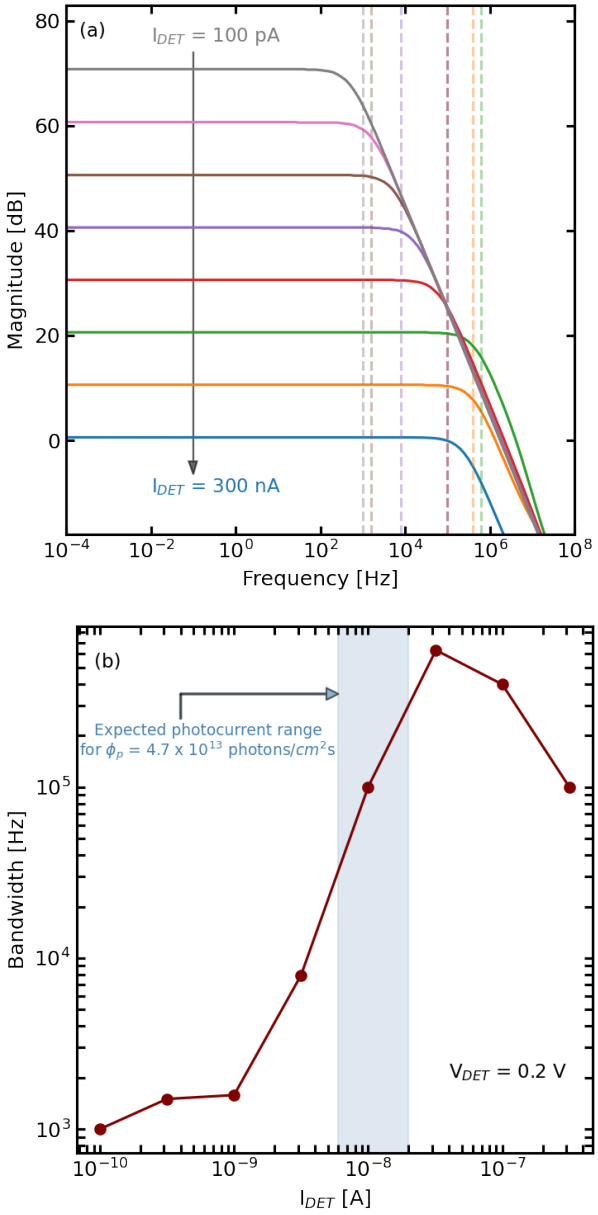

Figure 24: I_{DET} Bandwidth dependence (a) Bode plot shown at detector currents ranging from 100 pA to 300 nA with vertical lines represent the maximum gain minus 3 dB cutoff frequency (b) Cutoff frequencies extracted from fig 24-a plotted as a function of the corresponding detector current with a shaded region representing the expected range of photocurrents at -200 mV of bias.

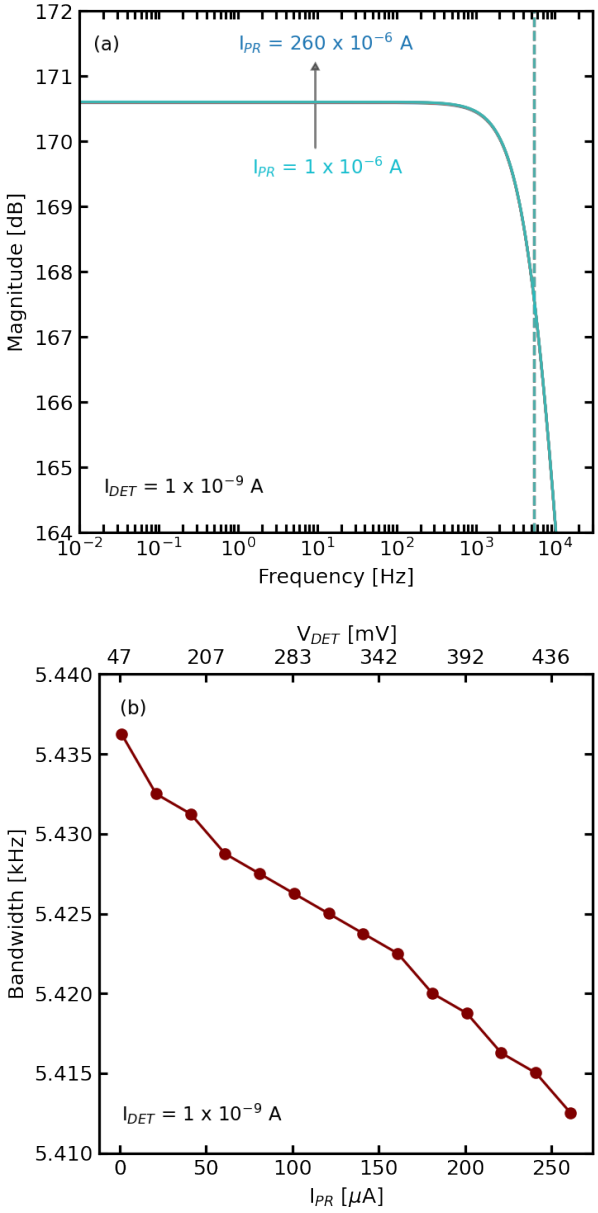

Figure 25: I_{PR} Bandwidth dependence (a) Bode plot shown at detector biasing currents ranging from 1 μA to 300 μA with vertical lines represent the maximum gain minus 3 dB cutoff frequency (b) Cutoff frequencies extracted from fig 24-a plotted as a function of the detector biasing currents on the bottom x-axis, with its' corresponding detector biasing voltages on the top x-axis.

5.4 Elmore Delay

A quick, commonly used method to estimate and approximate delay from the circuit, through an RC network as shown in the schematic presented in Fig. 26. The method is to transform each transistor into its equivalent resistor and capacitor to analyze then the shortest path from the input of the equivalent circuit to the output using (23).

$$t_{DELAY} = 0.69\tau_{eff} \tag{23}$$

Where the effective time constant τ_{eff} is the product of the feedback resistor R_{FB} equivalent to r_{ofb} and capacitor C_{FB} . Here again, we can use the channel length modulation effect to alter the time delay as well as use the transistor capacitance itself.

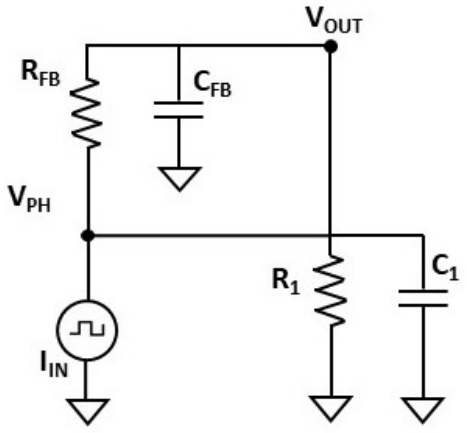

Figure 26: Elmore Delay equivalent circuit from the photoreceptor

6 Future Work

Future work will focus on, first, the analysis of the remaining stages of the EBS pixel circuitry, to simulate the response of the full circuit using T-SPICE and account for other possible limitations such as noise. Second, print the three stages on a PCB (Printable Circuit Board) to assess the performance using the setup discussed in Section 2.3 with varying input light levels to verify expected operation. Additionally, explore different configurations of the photoreceptor stage such as the common-source amplifier and study other operation regimes to optimize the designs and further improve the specs before creating the EBS-IR focal plane array.

REFERENCES

[1] S. Kleinfelder, S. Lim, X. Q. Liu, and A. El Gamal, "A 10000 frames/s cmos digital pixel sensor," IEEE J. Solid-State Circuits, vol. 36, no. 12, pp. 2049–2059, Dec. 2001.

[2] T. Delbruck and P. Lichtsteiner, "Fast sensory motor control based on event-based hybrid neuromorphic-procedural system," 2007 IEEE International Symposium on Circuits and Systems, New Orleans, LA, USA, 2007, pp. 845-848, doi: 10.1109/ISCAS.2007.378038.

[3] M. Loose, K. Meier, and J. Schemmel, "A self-calibrating single-chip cmos camera with logarithmic response," IEEE J. Solid-State Circuits, vol. 36, no. 4, pp. 586–596, Apr. 2001

[4] P. Lichtsteiner, C. Posch, and T. Delbruck, "A 128× 128 120 db 15 s latency asynchronous temporal contrast vision sensor," IEEE J. Solid-State Circuits, vol. 46, no. 2, pp. 566–576, Feb. 2008.

[5] S. Kavadias, B. Dierickx, D. Scheffer, A. Alaerts, D. Uwaerts, and J. Bogaerts, "A logarithmic response cmos image sensor with on-chip calibration," IEEE J. Solid-State Circuits, vol. 35, no. 8, pp. 1146–1152, Aug. 2000.

[6] T. Delbruck and C. A. Mead, "Analog vlsi adaptive logarithmic wide dynamic- range photoreceptor," Proc. IEEE ISCAS, pp. 339–342, May.1994.

[7] Katz, Nicholas M. "Nilpotent connections and the monodromy theorem: Applications of a result of Turrittin." Publications mathématiques de l'IHES 39 (1970): 175-232.

[8] Tanner™ T-Spice™ User's and Reference Manual, SIEMENS EDA, 2021.2, unpublished work. accessed through the software.

[9] W. E. Tennant, "'Rule 07' Revisited: Still a good heuristic predictor of p/n HgCdTe photodiode performance," J. Electron. Mater., vol. 39, no. 7, pp. 1030–1035, 2010

[10] A. T. Newell, J. V. Logan, R. A. Carrasco, Z. M. Alsaad, C. P. Hains, J. M. Duran, G. Ariyawansa, G. Balakrishnan, D. Maestas, C. P. Morath, P. T. Webster, Effects of doping and minority carrier lifetime on mid-wave infrared InGaAs/InAsSb superlattice nBn detector performance, Applied Physics Letters,2023

[11] Ning, Y. Taur and T.H, Fundamentals of Modern VLSI Devices, Cambridge University Press, 2009.

[12] C. -t. Sah, R. N. Noyce and W. Shockley, "Carrier Generation and Recombination in P-N Junctions and P-N Junction Characteristics," in Proceedings of the IRE, vol. 45, no. 9, pp. 1228-1243, Sept. 1957, doi: 10.1109/JRPROC.1957.278528.

[13] M. A. Kinch, Fundamentals of infrared detector materials. Bellingham, WA: SPIE Press, 2007.

[14] Sedra A. S. and Smith K. C. (1982). Microelectronic circuits. Holt Rinehart and Winston.

[15] S. Maimon and G. W. Wicks, "nBn detector, an infrared detector with reduced dark current and higher operating temperature," Appl. Phys. Lett, vol. 89, pp. 151109-1 - 151109-3, 2006

[16] R. A. Carrasco, A. T. Newell, Z. M. Alsaad, J. V. Logan, J. M. Duran, G. Ariyawansa, B. Pinkie, C. P. Morath, and P. T. Webster, "Capacitance–voltage modeling of mid-wavelength infrared nbn detectors," Journal of Applied Physics, vol. 133, no. 10, p. 104503, 2023.

[17] E. P. Vandamme, Ph. Jansen, L. Deferm, "Modeling the Subthreshold Swing in MOSFET's," IEEE Electron Device Letters, vol. 18, no. 8, August 1997.